Alternating Source-Detector Array Stationary CT System and Its Reconstruction

Authors: Dr. Jiabing Xiang, Wang, Yanxin, Yang, Yuhang, Prof. Wei Zhao, Li, Dr. Baolei, Sun, Dr. Bao-Hua, Sun, Dr. Bao-Hua

Date: 2025-11-02T00:00:00+00:00

Abstract

In this paper, we propose a novel design for a stationary CT system, termed the Alternating Source-Detector Array stationary CT (ASDA-sCT). The ASDA-sCT system comprises an array of miniature carbon nanotube X-ray sources and a detector array strategically positioned in the gaps between sources. To minimize projection loss caused by ray path obstruction, the X-ray sources are distributed within a short-scan trajectory that takes advantage of the fan-beam symmetry. After interpolation-based restoration of the discontinuities, CT images can be directly reconstructed using the filtered backprojection (FBP) algorithm with Parker' s weighting function. We further investigate the influence of the number of X-ray sources on the reconstruction quality of the ASDA-sCT system and determine the optimal source number for different X-ray exit window sizes. However, the limited number of sources and the interpolation errors introduced during sinogram restoration remain critical barriers to achieving high-quality image reconstruction. To tackle these issues, we propose a tailored triple-stage dual-domain cascade neural network (TSDDC-Net), which incorporates prior knowledge to correct interpolation errors in the sinogram and compensate for the missing projection views. In the projection domain, we introduce a novel multi-scale deformable convolution module (DFInception) that enhances feature extraction and improves the accuracy of sinogram refinement. In the image domain, a dual-encoder architecture is employed to independently extract features from the initial CT image reconstructed from raw interpolated projections and from the refined CT image reconstructed using the corrected sinogram. Ultimately, the well-designed deep learning model significantly enhances the quality of the reconstructed images. Experiments conducted on the Shepp-Logan phantom and abdominal CT datasets demonstrate the promising potential of the ASDA-sCT system for practical applications.

Full Text

Preamble

Alternating Source-Detector Array Stationary CT System and Its Reconstruction∗

Jia-bing Xiang,1 Yan-xin Wang,2 Yu-hang Yang,1 Wei Zhao,1, 3 Bao-lei Li,4, † and Bao-hua Sun1, ‡

1School of Physics, Beihang University, Beijing, 100191, China 2Hangzhou International Innovation Institute of Beihang, Beihang University, Hangzhou, 311115, China 3Tianmushan Laboratory, Hangzhou, 311115, China 4Beijing Hangxing Machinery Co.,Ltd., Beijing, 100013, China

In this paper, we propose a novel design for a stationary CT system, termed the Alternating Source-Detector Array stationary CT (ASDA-sCT). The ASDA-sCT system comprises an array of miniature carbon nanotube X-ray sources and a detector array strategically positioned in the gaps between sources. To minimize projection loss caused by ray path obstruction, the X-ray sources are distributed within a short-scan trajectory that takes advantage of the fan-beam symmetry. After interpolation-based restoration of the discontinuities, CT images can be directly reconstructed using the filtered backprojection (FBP) algorithm with Parker' s weighting function. We further investigate the influence of the number of X-ray sources on the reconstruction quality of the ASDA-sCT system and determine the optimal source number for different X-ray exit window sizes. However, the limited number of sources and the interpolation errors introduced during sinogram restoration remain critical barriers to achieving high-quality image reconstruction. To tackle these issues, we propose a tailored triple-stage dual-domain cascade neural network (TSDDC-Net), which incorporates prior knowledge to correct interpolation errors in the sinogram and compensate for the missing projection views. In the projection domain, we introduce a novel multi-scale deformable convolution module (DFInception) that enhances feature extraction and improves the accuracy of sinogram refinement. In the image domain, a dual-encoder architecture is employed to independently extract features from the initial CT image reconstructed from raw interpolated projections and from the refined CT image reconstructed using the corrected sinogram. Ultimately, the well-designed deep learning model significantly enhances the quality of the reconstructed images. Experiments conducted on the Shepp-Logan phantom and abdominal CT datasets demonstrate the promising potential of the ASDA-sCT system for practical applications.

Keywords: Computed Tomography, Stationary CT, Sparse-view CT, Deep learning

INTRODUCTION

Computed tomography (CT) is an imaging technique that reconstructs cross-sectional images of the interior of a body or object by measuring X-ray projections from multiple views with computational algorithms. Due to its ability to reconstruct high-resolution three-dimensional images, CT is widely used in medical diagnostics and industrial non-destructive testing. Currently, all modern CT scanners adopt the third-generation rotate-rotate geometry where a single or double X-ray sources with detector modules rotate around the object for a full 360-degree scan [1, 2]. The development of CT technology focuses on three key advancements: enhancing temporal resolution, reducing X-ray radiation exposure, and minimizing manufacturing costs [3]. However, the rotating mechanical structure of modern CT scanners constrains the further evolution of CT technology. Due to enormously increasing centrifugal forces, the rotational scan time of CT' s gantry has reached its limit of 0.25 seconds [2]. Meanwhile, vibrations in the CT acquisition system caused by mechanical rotation increase system noise and deteriorate the spatial resolution of CT images. Last but not least, the cumbersome gantry and complex dynamic acquisition mechanism not only hinder portability but also significantly increase manufacturing costs.

In the 1980s, electron beam CT (EBCT) scanners were developed with a stationary design, eliminating mechanical motion to achieve shorter scan times of 33 to 100 ms for cardiac imaging [1]. Nevertheless, the considerable expense associated with its production has confined EBCT exclusively to laboratory research. With continuous development in X-ray source technology, the size of X-ray sources has gradually reduced to the millimeter scale. Currently, miniature X-ray sources can be classified based on electron generation methods into thermal cathode X-ray sources [6, 7] and field emission cold cathode X-ray sources [8, 9, 12]. Miniature X-ray sources with thermal cathode still rely on high-temperature heating of cathode materials to emit electrons, resulting in a long switching response time and limiting their performance in high-speed dynamical applications. In contrast, miniature X-ray sources with field emission cold cathode constructed from nanomaterials such as carbon nanotubes (CNTs) offer significant advantages: they enable further miniaturization, operate with lower power consumption, and achieve substantially shorter switching response times. Recent studies have demonstrated that active-current control schemes can accelerate the response of CNT emitters to the tens-of-nanoseconds range, thereby enabling blur-free, high-frame-rate imaging [11]. In practical medical implementations, such as the stationary digital breast tomosynthesis system [10], a sealed 31-source CNT X-ray tube has achieved tube currents up to 38 mA and anode voltages up to 50 kVp. Long-term evaluations have confirmed stable performance, with a typical clinical lifetime exceeding three years under routine duty cycles. Collectively, these advantages make field emission X-ray sources highly promising for applications in medical imaging and industrial non-destructive testing.

With the advancement of field emission cold cathodes, the practical application of stationary CT systems composed of multiple sources has become feasible. A stationary CT scanner arranges multiple fixed X-ray sources around the scanned object and achieves X-ray projection acquisition from different angles by rapidly switching X-ray sources through electronic control. Therefore, stationary CT scanners overcome the constraints of centrifugal force and enable faster scanning speed without the dynamic rotation of the X-ray source and detector. The CNT X-ray source array was first applied to stationary chest tomosynthesis and successfully reduced motion artifacts in conventional tomosynthesis [13-15]. Compared to stationary chest tomosynthesis, stationary CT imaging is far more complex than simply replacing the rotating X-ray tube with a stationary CNT X-ray source array. Since CT imaging requires nearly full-angle (360°) projection data, the fixed geometry of both the X-ray sources and the detector module inevitably leads to X-ray path obstruction issues where the ray path may be obstructed by either the source array or the detector array. Enzhuo et al. [18] designed rotation-free square and hexagonal stationary micro-CT systems. Two or three contiguous linear source arrays, combined with two or three linear detector arrays, form a square or hexagonal geometry. In this geometry design, the scan angle range was limited to approximately 180°, and the CT image was reconstructed using an iterative reconstruction algorithm. Chen et al. [19] proposed a helical interlaced source-detector array CT architecture utilizing cylindrically distributed sources and a detector array. The missing data caused by source obstruction was compensated using interpolation, and a Katsevich-type reconstruction was implemented for fast approximate image reconstruction. Bossuyt et al. [20] developed a rectangular multi-source X-ray cargo scanning system, where multiple fixed X-ray sources arranged in a rectangular geometry provide multi-view projections without mechanical motion. A model-based iterative reconstruction algorithm was employed to suppress aliasing artifacts for material discrimination in cargo inspection. Gonzales et al. [21] introduced a multi-plane scanning scheme for baggage screening, in which two pairs of linear source arrays and detector arrays are positioned in two separate transverse planes while the screened object moves along the z-axis. Due to the noncircular and limited-angle scanning trajectory, CT reconstruction was performed using an accelerated compressed sensing algorithm, and an analytical reconstruction algorithm for this geometric configuration was provided in [5]. Similarly, a three-plane stationary CT prototype was developed and experimentally demonstrated to meet the requirements for head CT imaging [22]. To obtain complete and full-angle projection data without missing information, Thompson et al. [17] developed a source-detector double-ring configuration. The source-detector double-ring configuration consists of a source ring and a detector ring with a slight offset in the z-axial direction to avoid ray path obstruction. Although this geometric configuration enables the acquisition of projections from full angles, the geometric deviations caused by tilted scanning can result in artifacts in the reconstructed images.

Due to incomplete projection data caused by non-ideal scanning trajectories (e.g., sparse-view or limited-angle acquisitions) or ray path obstructions in stationary CT systems, conventional analytical reconstruction methods (filtered back-projection algorithm [23], FBP) are often inapplicable. Although iterative algorithms [24, 25] can reconstruct images from such incomplete data, their high computational complexity makes them impractical for real-time imaging applications, such as security screening and industrial non-destructive testing. Recently, the advent of the data-driven deep learning paradigm [26, 27] has revolutionized CT reconstruction by enabling faster reconstruction, enhancing image quality, and demonstrating great potential in mitigating artifacts caused by incomplete projection data. Deep learning can compensate for missing information caused by undersampling and limited angles by learning prior knowledge of the scanned object from a vast amount of data. Deep learning-based reconstruction methods can be categorized into three types based on the target domain: direct sinogram restoration in the projection domain [28–31], artifact correction in the image domain [32–37], and dual-domain joint optimization models that integrate information from both the projection and image domains [38–44]. Deep learning demonstrates strong potential for mitigating projection incompleteness in stationary CT systems through the integration of prior knowledge. Developing deep learning reconstruction frameworks customized for the geometry and sampling characteristics of stationary CT systems remains a valuable and critical research direction.

In this work, we propose a new design of a stationary CT system (Alternating Source-Detector Array stationary CT, ASDA-sCT) where the X-ray sources and detectors are alternately arranged on a circular ring. Since detectors are embedded between the X-ray sources, projection data occluded by the sources can be approximately recovered via interpolation from adjacent detector signals. The restored sinogram can then be used directly to reconstruct CT images using the filtered backprojection algorithm. To ensure projection angular coverage while minimizing projection loss due to source occlusion, the system adopts a short-scan acquisition mode. Through simulation experiments, we investigate the optimal number of X-ray sources for different exit window sizes. Beyond reconstructions using analytical and iterative methods, we also introduce a tailored deep learning framework designed to restore projection discontinuities and correct undersampling artifacts inherent to the ASDA-sCT system. We explore the optimal configuration of the X-ray source number and conduct a comprehensive comparison among analytical, iterative, and deep learning reconstruction methods. These experiments validate the practical feasibility and superior reconstruction capability of the proposed system.

Our contributions are outlined as follows: • We propose a novel stationary CT design (ASDA-sCT) with alternating X-ray sources and detectors on a circular ring with a short scan mode. • The design of the ASDA-sCT system enables convenient application of the analytical reconstruction algorithm. Through simulation experiments, we investigate the effects of X-ray source number and X-ray exit window size on reconstruction quality and determine the optimal source configuration. • We propose a three-stage dual-domain cascade network model tailored for the ASDA-sCT system. The model incorporates a novel

DFInception module to enhance feature extraction in the projection domain. In the image domain, a dual-encoder architecture is used to better fuse information from both initial and refined reconstructions. These innovations effectively improve the quality of the reconstructed images.

The remaining content is organized as follows. In Section II, we provide a detailed description of the system design and present analytical, iterative, and deep learning-based reconstruction methods. Section III presents the experimental setup, results, and discussion. The conclusions are drawn in Section IV.

II. MATERIALS AND METHODS

A. System Description

In stationary CT systems, the fixed geometric configuration of X-ray sources and detectors inherently results in incomplete projection sampling. Specifically, full-angle scans suffer from unavoidable obstruction of ray paths by source or detector components, leading to missing projections and degraded reconstruction quality. To overcome these limitations, we propose the ASDA-sCT system employing a short-scan acquisition mode. The geometric configuration of ASDA-sCT is illustrated in [FIGURE:1]. X-ray sources are uniformly distributed along a circular arc spanning from 0 to $\pi + 2\gamma$m, where 2γm denotes the fan angle of sources. A complete set of short-scan projections is acquired by rapidly switching between the sources. The detector array is divided into two segments: a continuous detector array covers the angular range from $\pi + 2\gamma$m to 2π while an interleaved detector array is embedded in the gaps between the X-ray sources. The use of a short-scan acquisition mode in ASDA-sCT not only reduces projection data loss but also decreases the required number of X-ray sources and increases acquisition efficiency.

In the proposed ASDA-sCT system, a short-scan acquisition mode is adopted based on the geometric symmetry of fan-beam projections, which ensures sufficient angular sampling for complete data acquisition with a scanning range of only $\pi + 2\gamma$m. Compared with a full 360° source arrangement, this configuration reduces the required number of X-ray sources for the same source density along the ring. Additionally, the detector segment without source placement can continuously measure projection data without interruption, thereby minimizing projection data loss. For regions with missing projection data, interpolation from adjacent detector signals can be used to estimate the absent measurements, thereby preventing the reconstruction task from degenerating into a limited-angle CT problem. [FIGURE:2] illustrates the 3D model of the proposed ASDA-sCT system, where the detector arrays are interleaved between adjacent X-ray sources. To minimize projection data loss at the source positions, each detector module is designed to cover as much of the gap between two neighboring sources as possible. Along the source array, only the X-ray exit windows are left uncovered, while all the remaining spaces between them are occupied by the detector arrays. Therefore, the size of each exit window corresponds to the spacing between adjacent detector arrays, which directly defines the regions of missing projections in the sinogram.

In summary, the ASDA-sCT geometry effectively mitigates the inherent ray-path obstruction problem in the design of stationary CT systems. However, projection discontinuities caused by source obstruction and artifacts from sparse angular sampling are still protogenetic issues for practical application. Hence, we focus on advancing the reconstruction algorithm to improve image quality under these constraints.

B. System Parameters

The geometric configuration of the ASDA-sCT system is summarized in . The system utilizes miniature CNT X-ray sources with a fan angle of 60° (half-angle γm = 30°), uniformly distributed along a circular detector ring with a radius of 512 mm. This setup provides an effective field of view (FOV) diameter of 512 mm, adequately satisfying the imaging requirements of both medical diagnostics and security screening applications.

In the ASDA-sCT system, imaging quality is strongly influenced by the size of the X-ray exit window and the number of X-ray sources. Due to ray path obstruction, detectors cannot be positioned within the exit window region, resulting in missing projection data where the sources occupy space on the detector ring. As the X-ray exit window size increases, the available detector area within the source-detector alternating segment decreases, causing a larger fraction of projections to be lost. The proportion of missing projections can be quantified as: deleted (= (2γm + π)R where N is the number of X-ray sources, s is the size of the X-ray exit window, R is the radius of the detector ring, and L is the arc length of the source-detector alternating segment.

When the sources fully occupy this segment (= 100%), all projection data in that region are lost, and the reconstruction task deteriorates into a limited-angle problem. Moreover, the exit window size constrains the maximum number of deployable sources, which can be estimated as: deleted (Nmax = (cid:22) (2γm + π)R (cid:23) · max where max denotes the maximum acceptable proportion of missing projections. Since the X-ray sources and detectors are alternately arranged, the number of X-ray sources and detectors is identical within each alternating segment: d + s (2γm + π)R d + s where N is the number of X-ray sources, d is the size of the detector array between adjacent sources, s is the size of the X-ray exit window, R is the radius of the detector ring, and L is the arc length of the source-detector alternating segment.

In this study, we consider three configurations with X-ray exit window sizes of 5 mm, 10 mm, and 20 mm. As illustrated in [FIGURE:3], the proportion of missing projections increases linearly with the number of sources. Taking into account the non-negligible size of detectors embedded between the sources, we set the maximum tolerable projection loss proportion to 90%. As illustrated in

Fig. 3, as the number of X-ray sources increases, the size of the detector array correspondingly decreases. For a fixed window size, the maximum number of deployable sources is determined by the minimum acceptable detector array size that can be placed between adjacent sources:

Nmax = (cid:22) $(2\gamma\mathrm{m} + \pi)$R dmin + s (cid:23)

Since the detector width cannot be infinitely small, we set the minimum detector array size to 1 mm, based on the current detector fabrication capabilities. Under this constraint, the maximum number of deployable sources is 357, 194, and 102 for window sizes of 5 mm, 10 mm, and 20 mm, respectively.

The number of X-ray sources plays a pivotal role in determining image reconstruction quality. A smaller number of sources reduces projection loss but may lead to insufficient angular sampling, resulting in pronounced aliasing artifacts. Conversely, increasing the number of sources enhances the projection number but exacerbates projection loss, potentially degrading reconstruction quality due to increased interpolation errors. Therefore, achieving an optimal balance between source number and projection completeness is essential in ASDA-sCT system design and will be further investigated in Sec. III.

C. Analytic Reconstruction using Parker’ s Smooth Weighting Function

Based on the geometric symmetry of the fan-beam, symmetric projection paths satisfy the following relationship: $\mathrm{p}(\gamma, \beta) = \mathrm{p}(-\gamma, \pi + \beta + 2\gamma)$, where p denotes the line integral projection, γ represents the position in the detector coordinate, and β is the projection angle. In a full-angle circular trajectory fan-beam CT scan, each projection path is sampled twice. To eliminate redundant projections, the short-scan acquisition mode reduces the total scan angle from 2π to $\pi + 2\gamma\mathrm{m}$ without compromising the completeness of the projection data. The redundant projection region in a fan-beam short-scan sinogram is illustrated in FIGURE:4.

To avoid artifacts in the reconstructed image, sinogram redundancy must be reweighted to ensure that each ray contributes equally to the reconstructed image. This is achieved by applying a weighting function that equalizes the contribution of singly- and doubly-sampled projections. In this work, we adopt the smooth weighting function proposed by Parker [45]:

(cid:18) π $\gamma\mathrm{m} - \gamma$ (cid:19) $\omega\beta$ $(\gamma) =$ $0 \leq \beta < 2\gamma\mathrm{m} - 2\gamma$ $2\gamma\mathrm{m} - 2\gamma \leq \beta \leq \pi - 2\gamma$ (cid:18) π $\pi + 2\gamma\mathrm{m} - \beta$ $\gamma\mathrm{m} + \gamma$ (cid:19) $\pi - 2\gamma < \beta \leq \pi + 2\gamma\mathrm{m}$

The projections are then reweighted using this function, followed by image reconstruction via the filtered backprojection algorithm.

FIGURE:4 presents the measured sinogram from the ASDA-sCT system. Due to the absence of detectors at source positions, periodically spaced band-like gaps appear in the redundant region of the sinogram. Geometric ray path analysis reveals that X-rays emitted from a given source are lost when projected onto the position of an opposing X-ray source, where no detectors are present. Due to the reversibility of light paths, the conjugate rays traveling in the opposite direction are also missing. Consequently, the conjugate projection rays are missing in pairs, making it impossible to compensate for the loss solely through the arrangement of X-ray sources. To mitigate this discontinuity, linear interpolation using neighboring projection data can be applied to estimate the missing values.

D. Iterative Reconstruction Algorithms

Compared to the analytical reconstruction algorithm, iterative reconstruction methods offer greater flexibility in handling incomplete or non-uniform projection data. They enable stable image reconstruction under conditions such as sparse sampling or missing projections. Moreover, prior knowledge, such as non-negativity, total variation minimization, and sparsity, can be incorporated as regularization terms during the iterative process to improve reconstruction quality. The Simultaneous Algebraic Reconstruction Technique (SART) [51, 52] is one of the most widely used iterative algorithms. Unlike the Algebraic Reconstruction Technique (ART) [53], which updates pixel values sequentially for each ray, SART employs a block-wise update strategy. In each iteration, it computes corrections from all projection paths and averages them to update the image. The iterative update formula is given by:

Currently, x(k+1) = x(k) j + λ (cid:80)M (cid:17) (cid:16) pi− ai,x(k) ai 2 i=1 aij (cid:80)M

where x(k) denotes the value of pixel j at iteration k, pi is the measured projection for the i-th ray, ai is the i-th row of the system matrix, aij is its (i, j)-th entry, and λ is the relaxation parameter. By averaging over all projections, SART reduces the impact of local noise, thereby improving reconstruction stability.

To mitigate the undersampling issue in the ASDA-sCT system, a compressed sensing (CS)-based reconstruction method with total variation (TV) regularization can be employed. The reconstruction method is based on the Adaptive Steepest Descent -Projection onto Convex Sets (ASD-POCS) algorithm [54]. It minimizes the following objective function:

(cid:0) Ax − p 2 + α TV(x)(cid:1),

where A is the system matrix, p is the measured projection data, and α is the regularization weight. The TV term, TV(x), minimizes the 1-norm of the image gradient, encouraging piecewise-smooth structures and preserving sharp edges. ASD-POCS integrates gradient-based optimization with projection onto convex sets, ensuring convergence while enhancing image quality under sparse-view acquisition.

E. Deep Learning Reconstruction Method: A Three-Stage Dual-Domain Cascade Neural Network

The interpolation errors and the limited number of X-ray sources significantly degrade CT image reconstruction quality. Recently, data-driven deep learning methods have demonstrated strong potential in learning the underlying structure of scanned objects to compensate for the missing information caused by sinogram discontinuities and undersampling. Therefore, we propose a Three-Stage Dual-Domain Cascade neural network (TSDDC-Net) that incorporates prior knowledge to improve reconstruction quality. An overview of the proposed deep learning-based reconstruction framework is presented in [FIGURE:5].

Sinogram Restoration Upsampling In the first stage, linear interpolation is used to coarsely restore discontinuities in the measured sinogram. To alleviate undersampling artifacts, interpolation is also applied along the angular direction to enhance projection density. However, the coarse restoration upsampling process inevitably introduces substantial interpolation errors, which limit the quality of the reconstructed images. Thus, a subsequent correction stage is necessary to correct interpolation errors and improve image quality.

Sinogram-Domain Network In the second stage, a UNet-based Sinogram-Domain Network (SD-Net) is employed to correct interpolation errors in the sinogram. The network adopts the classical encoder-decoder structure, where multi-scale features are extracted and hierarchically upsampled to produce a refined sinogram. To enhance the network’ s feature extraction capability, we propose a Deformable Inception (DFInception) module, which integrates the deformable convolution [55] with the InceptionNext module [56, 57]. Deformable convolution introduces learnable offset parameters to the standard convolution operation, enabling the network to adjust the sampling locations of the convolutional kernels adaptively. This mechanism allows the receptive field to dynamically change its shape and position in response to the geometric structure of the input features. The deformable convolution operation can be expressed as:

Y (p0) = (cid:88) w(pn) · X(p0 + pn + Δpn),

where X and Y denote the input and output feature maps, respectively, p0 is the position of the current output location, R represents the receptive field of the convolution kernel, pn is the predefined offset of the n-th sampling point in R, w(pn) is kernel weight at position pn, and Δpn R2 is the learnable offset for sampling position pn. The core idea of the Inception module is to apply multiple convolutional filters with different kernel sizes in parallel within the same layer, enabling multi-scale feature extraction. The operation can be expressed as:

Y = X + Concat (cid:32) n (cid:88) (cid:33),

X = Concat(Xi), where the input feature map X is split into n channel groups Xi. Then, each Xi is processed by a deformable convolution f with kernel size ki. The outputs are then concatenated and added to the original input via a residual connection.

The design of the DFInception module is motivated by two key observations. First, sinogram data consist of overlapping sinusoidal trajectories, which inherently are global patterns across the entire image. Standard convolutional layers are limited to local receptive fields and thus struggle to capture such long-range dependencies. In contrast, our proposed DFInception module combines deformable convolutions and multi-scale kernels to effectively extend the receptive field and capture long-range interactions with significantly fewer parameters than Transformer-based models. Second, due to the large missing regions in sinograms, using elongated convolutional kernels (e.g., 1 × 11) is essential for enabling the network to directly connect the central pixels of the missing regions with the surrounding measured areas in the high-resolution layers of the UNet architecture. This facilitates early-stage compensation and significantly improves the performance of error correction.

When supervised by ground-truth well-sampled sinograms, SD-Net effectively learns to correct interpolation errors. The refined sinogram is subsequently reconstructed via the filtered backprojection algorithm to produce a refined CT image, which is then fed into the image-domain refinement stage. The network is trained using a mean squared error (MSE) loss:

LSD = ˆS − Sgt 2

where ˆS is the refined sinogram, and Sgt represents the ground truth.

Image-Domain Network Although sinogram-domain correction reduces major artifacts, even small residual errors in the sinogram can lead to noticeable artifacts in the reconstructed CT images, such as blurring, structural distortion, and loss of edge contrast. This observation highlights that prior knowledge in the sinogram domain alone is insufficient for high-fidelity reconstruction. To further enhance image quality, especially in terms of structural details and edge preservation, we introduce an Image-Domain refinement Network (ID-Net) designed to correct interpolation errors that remain unaddressed or are newly introduced in the sinogram domain.

The network is fed with two CT images: one reconstructed from the SD-Net-corrected sinogram and the other from the raw interpolated sinogram. In this way, prior knowledge introduced from the sinogram domain is effectively utilized while retaining the original measured information. Two separate encoders are employed to extract multi-scale features from both inputs, leveraging complementary information from sinogram correction and initial reconstruction. These features are then fused through a decoder to generate the final high-quality CT image. The network is supervised using CT images reconstructed from fully sampled sinograms, and trained with an MSE loss as well:

LID = ˆI − Igt 2

where ˆI denotes the predicted CT image, and Igt represents the ground truth.

F. Experiment Dataset

We evaluate the design of the ASDA-sCT and its reconstruction method using a Shepp-Logan phantom and a publicly available abdominal CT dataset, authorized for the 2016 NIH-AAPM-Mayo Clinic Low Dose CT Grand Challenge by Mayo Clinic. In this dataset, 6146 full dose abdominal CT 2D slices from 42 anonymous patients are divided into a training set of 4138 CT images (27 patients), a validating set of 625 CT images (5 patients), and a testing set of 1356 CT images (10 patients) with 70% allocated for training, 10% allocating for validating, and 20% for testing. Before training, the CT images and projections are normalized into [0,1]. The photon number was set to 1 × 107 in the simulation. The number of iterations was set to 200 for both SART and POCS-TV. The regularization weight α in POCS-TV was set to 1. SD-Net and ID-Net were trained for 200 epochs with an initial learning rate of 0.0005. The system configuration is listed in . All experiments were run on a computer with an Intel(R) Xeon(R) Silver 4210R CPU and an NVIDIA GeForce GTX3090.

III. RESULTS AND DISCUSSION

A. Find The Optimal Source Number

In this study, we conducted simulated reconstruction experiments using the training dataset CT images under different numbers of X-ray sources, followed by a quantitative evaluation of the reconstruction results shown in [FIGURE:7]. The experiments compared the reconstructed images from ASDA-sCT systems with different exit window sizes to those from sparse-view CT systems with the same number of sources but without sinogram discontinuities. The results demonstrate that both the number of sources and the size of the exit window are critical factors influencing reconstruction quality. In the ASDA-sCT system, the number of X-ray sources is limited by the physical size of the CNT X-ray sources. For the smallest exit window size in our simulation (5 mm), the total number of X-ray sources can reach only about 357. Therefore, for medical diagnostic applications, the number of projection views in ASDA-sCT falls below the Nyquist sampling requirement, which may lead to angular aliasing and degradation of fine structural and lesion details in the reconstructed images. This undersampling issue must be addressed by advanced reconstruction algorithms to enable practical clinical implementation.

When the number of sources is under 50, the reconstruction quality of the stationary CT system is comparable to that of the sparse-view CT system. In this case, image degradation is mainly due to aliasing artifacts caused by undersampling. As the number of sources increases, the reconstruction quality gradually improves. However, the improvement in the stationary CT system is less than that in the sparse-view CT system, primarily because interpolation errors become more pronounced due to increased projection loss.

The study further reveals that the size of the source window has a substantial impact on reconstruction quality. Larger window sizes necessitate interpolation over broader regions, which increases interpolation errors. Consequently, for a fixed number of sources, systems with smaller window sizes yield lower interpolation errors and achieve better reconstruction quality. Remarkably, when the window size is reduced to 5mm, the reconstruction quality of the stationary CT system becomes closely comparable to that of the sparse-view CT system with the same number of sources. This finding suggests that further reduction in source size could effectively suppress interpolation artifacts, enabling the stationary CT system to achieve image quality comparable to that of rotating CT systems, while avoiding projection loss caused by ray path obstruction.

Overall, although increasing the number of sources exacerbates interpolation errors, it more effectively mitigates the dominant aliasing artifacts caused by undersampling. Therefore, the optimal number of sources in the ASDA-sCT system should be maximized within the physical constraints of X-ray source placement. Specifically, the experimental results indicate that when the maximum allowed proportion of missing projections is set to 90% and the minimum detector array size is set to 1mm, the optimal number of sources for exit window sizes of 5mm, 10mm and 20mm is 357, 194 and 102, respectively.

B. Experiments on the Shepp-Logan Phantom

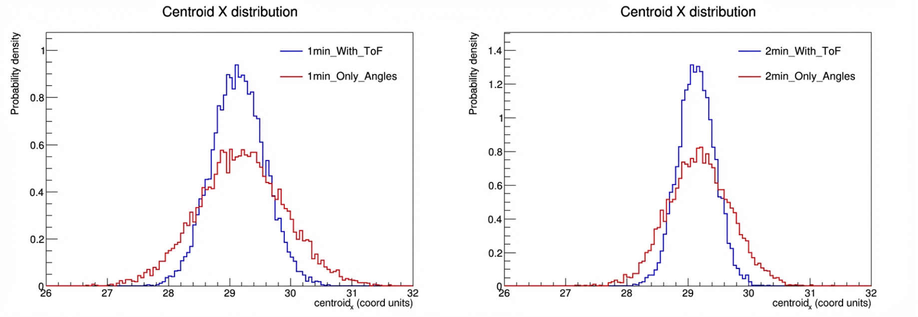

Figure 1: Figure 8

illustrates the measured sinograms of the ASDA-sCT system under different X-ray exit window sizes. In the upper and lower triangular regions of the sinogram, known as ray-redundant regions, strip-like gaps appear due to the lack of detector coverage at source positions. For all three systems, with optimal numbers of X-ray sources corresponding to window sizes of 5mm, 10mm, and 20mm, the proportion of missing projections in the redundant ray regions is approximately 90%, as previously specified. Larger exit window sizes result in wider projection gaps and a greater number of missing pixels requiring interpolation, which in turn leads to increased interpolation errors. Conversely, smaller window sizes allow for the deployment of more X-ray sources within the same scanning trajectory. This not only reduces aliasing artifacts but also decreases interpolation errors as well.

To roughly recover the missing projection data, linear interpolation is applied based on the available neighboring signals within each source gap. This approach performs well in regions where the projection values change gradually. However, in areas with large projection gradients, typically corresponding to structural edges in the image, linear interpolation introduces significant errors. Such errors not only contribute to visible artifacts but also degrade the accuracy of edge representation and structural detail in the final reconstructed images. However, in regions with large projection gradients—such as those indicated by the red arrows in the interpolation error images of

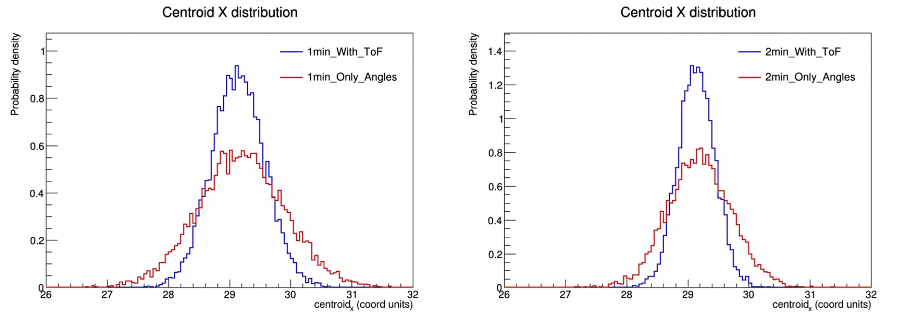

Figure 2: Figure 8

—linear interpolation introduces substantial errors. These areas correspond to the edges of the outer elliptical structure in the reconstructed images, as highlighted by the red arrows in the residual images of [FIGURE:9] (third column). Consequently, the introduced interpolation errors primarily degrade the accuracy of edge reconstruction and increase visible artifacts in the reconstructed images.

[FIGURE:9] shows the reconstruction results of the Shepp-Logan phantom using both analytical and iterative methods. Compared with results from sparse-view CT, ASDA-sCT reconstructions exhibit not only aliasing artifacts but also more pronounced errors near edge structures due to interpolation inaccuracies. As the exit window size decreases, the system accommodates more sources, thereby reducing both aliasing and interpolation-related artifacts. Although iterative algorithms such as SART and POCS-TV can effectively suppress aliasing artifacts, such methods entail increased computational complexity and substantial reconstruction time. [FIGURE:9] presents a comparison between the reconstruction results of the Shepp-Logan phantom obtained from the ASDA-sCT system and those reconstructed from a conventional rotational CT (sparse-view CT) with the same scanning configuration. For the sparse-view rotational CT, the differences from the ground truth primarily arise from streaking aliasing artifacts caused by insufficient projection sampling. In contrast, the ASDA-sCT reconstructions exhibit not only aliasing artifacts but also pronounced edge errors at the edge of the reconstructed object, which are attributed to interpolation inaccuracies in the sinogram. Among the three reconstruction methods, the FBP algorithm is inherently less stable and tends to be sensitive to local interpolation errors in the sinogram and the undersampling issue. The SART method is able to partially suppress aliasing artifacts by ensuring projection consistency. The POCS-TV algorithm yields the best performance, as its total variation prior—assuming gradient sparsity—matches the piecewise-smooth characteristics of the Shepp–Logan phantom, resulting in minimal aliasing artifacts and edge errors. As the exit window size decreases, more X-ray sources can be accommodated within the same scanning trajectory, thereby increasing the number of available projections and reducing aliasing artifacts. Meanwhile, a smaller exit window size also narrows the missing projection regions, which enhances interpolation accuracy in the sinogram and consequently improves the fidelity of edge reconstruction. summarizes the quantitative evaluation results for the Shepp–Logan phantom experiments. Consistent with the observations in [FIGURE:9], the POCS-TV algorithm achieves the best quantitative results due to its effective use of prior information. All three reconstruction methods show improved performance as the exit window size decreases, benefiting from increased sampling and reduced interpolation errors.

C. Experiments on the Abdominal CT Dataset

[FIGURE:10], [FIGURE:11], and [FIGURE:12] present abdominal CT reconstruction results obtained using FBP, iterative reconstruction, and deep learning methods under X-ray exit window sizes of 5 mm, 10 mm, and 20 mm, respectively. Although the FBP algorithm provides the fastest reconstruction speed, it yields the worst image quality. As shown in the enlarged view of the red-box region in FIGURE:12 (yellow arrows), the anatomical details of the soft tissue are almost indistinguishable due to the mixture of severe aliasing artifacts and interpolation errors. As shown by the quantitative results in , the reconstruction performance of SART is only slightly better than that of FBP. Visually, the differences between the two reconstructions are minimal, with almost no noticeable improvement.

Among traditional methods, the POCS-TV algorithm, which incorporates total variation regularization, achieves more effective suppression of aliasing artifacts. However, the strong regularization constraint leads to the over-smoothing problem. As observed in FIGURE:12, the internal cavities and fine structural features of the soft tissue are oversmoothed. The gray-level transitions become overly uniform, and most texture details are lost, producing a plastic- or wax-like appearance, commonly named as plastic-like artifacts. Such excessive smoothing often results in a lack of fine texture details, which may reduce the diagnostic reliability of the reconstructed image.

In contrast, data-driven deep learning methods exhibit incomparable advantages in both artifact suppression and structural detail preservation. As illustrated in

Figs. 10(b,*), 11(b,*), and 12(b,*), the reconstruction residuals of deep learning-based methods are significantly smaller than those of traditional algorithms. also demonstrates that when facing severe artifacts (at exit window sizes of 10 mm and 20 mm), deep learning methods achieve substantial improvements in reconstruction accuracy. This advantage stems from their ability to exploit learned statistical priors of the scanned objects, thereby achieving more effective artifact suppression and enhanced preservation of structural details. We compared three representative deep learning models—FBPConvNet [32], HD-Net [43], and DuDoTrans [44]. For comparison, three representative deep learning models—FBPConvNet [32], HD-Net [43], and DuDoTrans [44]—were evaluated alongside our proposed TSDD-Net model under the same experimental conditions. All models were trained on the same dataset with their respective optimal training configurations as reported in the original publications. The image-domain-only model FBPConvNet still struggles with limited edge sharpness and incomplete recovery of fine structures. By comparison, models such as HD-Net, DuDoTrans, and the proposed TSDDC-Net, which incorporate prior knowledge from both projection and image domains, demonstrate substantially improved reconstruction performance. Among them, TSDDC-Net consistently achieves the best results in minimizing artifacts while preserving fine anatomical details. As shown in FIGURE:11, FBPConvNet is capable of reconstructing most of the soft-tissue details. However, the internal cavity boundaries are not clearly reconstructed, and the streak-like structures indicated by the bottom yellow arrow appear blurred. HD-Net, which integrates domain priors from both the projection and image domains, delivers notably superior reconstruction results compared with FBPConvNet. The reconstruction obtained by HD-Net exhibits enhanced clarity in soft-tissue contours. In comparison, DuDoTrans produces an overly smoothed reconstructed image, leading to a perceptible loss of high-frequency structural information. The proposed TSDDC-Net achieves the highest reconstruction accuracy, accurately recovering the soft-tissue morphology, delineating the boundaries of internal cavities, and preserving the streak-like textural features indicated by the yellow arrows. Overall, TSDDC-Net consistently achieves the best performance in minimizing artifacts while preserving fine anatomical details. This observation is further confirmed by the results shown in [FIGURE:10] and 12(c,*) for all compared methods.

When the system' s X-ray exit window size increases to 20mm, the reduced number of deployable X-ray sources leads to more severe interpolation errors and aliasing artifacts in the initial reconstruction image. As a result, the performance of all reconstruction methods noticeably degrades. Analytical and iterative methods, in particular, suffer from significant blurring and detail loss. For instance, the anatomical structures shown in FIGURE:12 become indistinct and barely recognizable. Among the deep learning methods, all comparison models exhibit noticeable structural degradation, struggling to recover fine details as well. In contrast, the proposed TSDDC-Net is able to preserve tissue boundaries and edge structures, demonstrating superior stability and robustness even under challenging ASDA-sCT system configurations with larger window sizes. These results demonstrate the superiority of our proposed TSDDC-Net, specifically designed for ASDA-sCT systems. For the system with an exit window size of 20 mm ([FIGURE:12]), the sparse angular sampling and large interpolation errors lead to severe detail loss in the reconstruction results of all three traditional methods. Although deep learning-based approaches can reconstruct the overall soft-tissue contours, the fine structural textures and the morphology of internal cavities are largely missing. When the exit window size decreases to 10 mm ([FIGURE:11]), the number of available projections increases. Therefore, all reconstruction methods show substantial improvement in image quality. Among them, the proposed TSDDC-Net achieves the best performance, with only minor detail loss observed in a few localized regions. As the exit window further narrows to 5 mm ([FIGURE:10]), the projection sampling becomes sufficiently dense and is no longer considered sparse. Under this condition, traditional methods can reconstruct almost complete structural details with minimal artifacts. Deep learning-based approaches further enhance image quality, producing reconstructions that closely match the ground truth (the fully sampled rotational CT image with N = 960) and exhibiting fidelity sufficient for clinical diagnostic applications.

In summary, the exit window size critically affects the performance of reconstruction methods for the ASDA-sCT system. Smaller window sizes enable denser projection sampling, leading to higher reconstruction fidelity. Deep learning methods, by leveraging learned prior knowledge, can effectively compensate for missing information caused by undersampling and further enhance image quality.

To further evaluate the effectiveness of the proposed dual-domain architecture, particularly the DFInception module in the projection domain and the dual-encoder design in the image domain, we conducted a series of ablation experiments, as presented in . The quantitative results in confirm that the proposed TSDDC-Net, incorporating our novel architectural components, achieves the best performance across all evaluation metrics. In the ablation experiments, we removed individual modules and compared the reconstruction performance before and after removal to verify their effectiveness in the network. The results reveal that models leveraging only single-domain priors, either the sinogram domain or the image domain, yield lower performance compared to the dual-domain model. The results in the first three rows of indicate that utilizing priors from only a single domain, whether the sinogram or the image domain, leads to inferior reconstruction performance compared to the dual-domain model. This demonstrates the effectiveness of jointly exploiting complementary information from both domains to achieve superior reconstruction quality. Specifically, the projection-domain-only model outperforms the image-domain-only model. The relatively smooth variations and simpler structural patterns in projection data make it easier for the model to learn and generalize. In contrast, image-domain data often exhibits complex aliasing, interpolation-induced artifacts, and noise, which substantially increase learning difficulty.

Furthermore, the incorporation of the DFInception module enhances the sinogram refinement capability in the projection domain, improving the quality of the refined CT image. Meanwhile, the dual-encoder design in the image domain effectively integrates complementary features from the initial reconstructed image and the SD-Net-refined image, leading to enhanced edge preservation and finer structural detail in the final reconstructed CT image.

D. Computational Efficiency

The deep learning-based methods offer another significant advantage—computational efficiency and parallelizability. presents a summary of the reconstruction time required by different methods for the ASDA-sCT system with an exit window size of 10 mm (N=194) under identical experimental settings (see Section II F). Each result is averaged over 500 random reconstruction runs. Among all methods, the FBP algorithm achieves the fastest speed but yields the lowest reconstruction quality. Both SART and POCS-TV algorithms require repeated iterations of forward and backward projecting, resulting in substantially increased computational costs. Consequently, these methods exhibit the slowest reconstruction speed. FBPConvNet achieves the fastest computational speed among the deep learning-based methods but yields the lowest reconstruction accuracy. DuDoTrans has a slower inference time because its Transformer-based architecture involves higher computational complexity and a larger number of parameters compared with convolutional networks. Between the two dual-domain convolutional networks, TSDDC-Net is slightly slower than HD-Net, but it achieves better reconstruction quality. Overall, TSDDC-Net enables near real-time reconstruction at sub-second speeds and demonstrates strong potential for real-time dynamic CT imaging applications.

IV. SUMMARY

This study proposes an Alternating Source-Detector Array Stationary CT (ASDA-sCT) system capable of tomographic imaging without gantry rotation. The system utilizes a computationally efficient interpolation strategy to complete missing projections, enabling direct reconstruction using the filtered backprojection algorithm. In the proposed design, maximizing the number of X-ray sources is crucial for achieving optimal reconstruction quality. Furthermore, we introduce TSDDC-Net, a deep learning reconstruction model specifically tailored for this system. By incorporating the novel DFInception feature extraction module and an advanced dual-domain architecture, TSDDC-Net effectively corrects interpolation errors and suppresses aliasing artifacts. Experimental results highlight the ASDA-sCT system' s strong potential in clinical imaging and industrial nondestructive testing.

The ASDA-sCT system offers diverse potential applications. By incorporating multi-row detectors and adopting a cone-beam CT (CBCT) geometry, the system can be configured into a stationary CBCT (sCBCT) system, effectively addressing the slow scanning speed of conventional CBCT. More importantly, sCBCT enables a nearly motion artifact-free real-time 4D dynamic reconstruction. To address undersampling challenges inherent in the ASDA-sCT system, we can increase the number of projections by employing a multi-plane scanning strategy. Each scanning plane is equipped with an ASDA-sCT scanner, capturing projections from different view angles. This design offers a promising solution for applying the ASDA-sCT system in industrial CT inspection and security screening.

Due to the large amount of CT data of anatomical structures available in clinical practice and the excellent performance of deep learning reconstruction, deep learning-based reconstruction methods are expected to facilitate the widespread clinical adoption of ASDA-sCT. The ASDA-sCT system acquires fewer projections, reducing radiation dose while maintaining diagnostic quality. In addition, its extremely fast scanning speed allows for imaging of rapidly moving objects, such as in cardiac CT imaging.

Nevertheless, certain fundamental challenges inherent to stationary CT remain unresolved. One prominent issue is X-ray scatter, which arises from the system’ s collimator-free design and leads to significant scatter-induced artifacts. Developing effective scatter correction strategies will be a critical and promising direction for future research in stationary CT system design. For ASDA-sCT, traditional correction methods such as scatter-kernel superposition [58] and Monte Carlo simulation-based models [59, 60] remain applicable, but their limited performance and high computational cost hinder clinical feasibility. Recent advances in deep-learning-based methods [61–63] have demonstrated superior performance in scatter correction, resulting in faster and more accurate results. Therefore, exploring deep learning frameworks that incorporate scatter artifact correction for ASDA-sCT will be an important and promising topic for future research.

References

[1] W.A. Kalender, X-ray computed tomography. Phys. Med. Biol., 51, 13 (2006). doi: 10.1088/0031-9155/51/13/R03 [2] J. Hsieh, T. Flohr, Computed tomography recent history and future perspectives. J. Med. Imaging, 8, 5:052109-052109 (2021). DOI: 10.1117/1.JMI.8.5.052109 [3] T.M. Buzug, Computed tomography, (Springer, Berlin Heidelberg, 2011), pp. 311-342. [4] C. Gong, L. Zeng, C. Wang, et al., Design and Simulation Study of a CNT-Based Multisource Cubical CT System for Dynamic Objects. Scanning, 2018, 1: 6985698 (2018). DOI: 10.1155/2018/6985698 [5] T. Zhang, Y.-X. Xing, L. Zhang, et al., Stationary computed tomography with source and detector in linear symmetric geometry: Direct filtered backprojection reconstruction. Med. Phys., 47, 5 (2020). DOI: 10.1002/mp.14058 [6] S. Cornaby, A. Reyes-Mena, P.W. Moody, et al., Simultaneous XRD/XRF with low-power X-ray tubes. Advances in X-ray Analysis: Proceedings of the Denver X-ray Conference, 45, 34 (2002). [7] G.-D. Anna, Miniature X-ray sources. J. Microelectromech. Syst., 26, 1 (2017). DOI: 10.1109/JMEMS.2016.2640344 [8] G.-Z. Yue, Q. Qiu, B. Gao, et

al., Generation of continuous and pulsed diagnostic imaging x-ray radiation using a carbon-nanotube-based field-emission cathode. Appl. Phys. Lett., 81, 2 (2002). DOI: 10.1063/1.1492305 [9] Y. Cheng, O. Zhou, Electron field emission from carbon nanotubes. C. R. Phys., 4, 9 (2003). DOI: 10.1016/S1631-0705(03)00103-8 [10] X. Qian, A. Tucker, E. Gidcumb, et al., High resolution stationary digital breast tomosynthesis using distributed carbon nanotube x-ray source array. Med. Phys., 39.4 (2012). DOI: 10.1118/1.3694667 [11] J. Kang, H. Lee, J. Jeong et al., Fast and Stable Operation of Carbon Nanotube Field-Emission X-Ray Tubes Achieved Using an Advanced Active-Current Control. IEEE Electron Device Lett., 36.11, (2015). DOI: 10.1109/LED.2015.2478157 [12] J. Zhang, G. Yang, Y. Cheng, et al., Stationary scanning x-ray source based on carbon nanotube field emitters. Appl. Phys. Lett., 86, 18 (2005). DOI: 10.1063/1.1923750 [13] J. Shan, P. Chtcheprov, A.W. Tucker, et al., Stationary chest tomosynthesis using a CNT x-ray source array. Medical Imaging 2013: Physics of Medical Imaging. 8668. (2013). [14] P.R. Schwoebel, J.M. Boone, and J. Shao, Studies of a prototype linear stationary x-ray source for tomosynthesis imaging. Phys. Med. Biol., 59, 10 (2014). DOI: 10.1088/0031-9155/59/10/2393 [15] J.S. Maltz, F. Sprenger, J. Fuerst, et al., Fixed gantry tomosynthesis system for radiation therapy image guidance based on a multiple source x-ray tube with carbon nanotube cathodes. Med. Phys., 36, 5 (2009). DOI: 10.1118/1.3110065 [16] C. Puett, C. Inscoe, A. Hartman, et al., An update on carbon nanotube-enabled X-ray sources for biomedical imaging. Wiley Interdiscip. Rev.-Nanomed. Nanobiotechnol., 10, 1 (2018). DOI: 10.1002/wnan.1475 [17] W.M. Thompson, W.R.B. Lionheart, E.J. Morton, et al., High speed imaging of dynamic processes with a switched source x-ray CT system. journal, Meas. Sci. Technol. 26. 5 (2015). DOI: 10.1088/0957-0233/26/5/055401 [18] E.M. Quan, D.S Lalush, Three-dimensional imaging properties of rotation-free square and hexagonal micro-CT systems. IEEE Trans. Med. Imaging, 29, 3 (2010). DOI: 10.1109/TMI.2009.2039799 [19] Y. Chen, Y. Xi, J. Zhao, A stationary computed tomography system with cylindrically distributed sources and detectors. J. X-Ray Sci. Technol., 22, 6 (2014). DOI: 10.3233/XST-140456 [20] C. Bossuyt, A.J. Dekker, D. Iuso, et al., Framework for optimal design of a multi-source rectangular X-ray cargo scanning system, Radiat. Phys. Chem., 239, 113332 (2025). DOI: 10.1016/j.radphyschem.2025.113332 [21] B. Gonzales, D. Spronk, Y. Cheng, et al., Rectangular fixed-gantry CT prototype: combining CNT X-ray sources and accelerated compressed sensing-based reconstruction. IEEE Access, 2 (2014). DOI: 10.1109/ACCESS.2014.2351751 [22] E. Spronk, Y.T. Luo, C.R. Christina, et al., Evaluation of carbon nanotube x-ray source array for stationary head computed tomography. Med. Phys., 48, 3 (2021). DOI: 10.1002/mp.14696 [23] L. Shepp, B.F. Logan, The Fourier reconstruction of a head section. IEEE Trans. Nucl. Sci., 21, 3 (1974). DOI: 10.1109/TNS.1974.6499235 [24] M. Beister, D. Kolditz, W.A. Kalender, Iterative reconstruction methods in X-ray CT. Phys. Medica, 28, 2 (2012). DOI: 10.1016/j.ejmp.2012.01.003 [25] M.J. Willemink, P.A. de Jong, T. Leiner, et al., Iterative reconstruction techniques for computed tomography Part 1: technical principles. Eur. Radiol., 23 (2013). DOI: 10.1007/s00330-012-2765-y [26] Y. LeCun, Y. Bengio, G. Hinton, et al., Deep learning. Nature, 521, 7553 (2015). DOI: 10.1038/nature14539 [27] D.G. Shen, G.R. Wu, H.I. Suk, Deep learning in medical image analysis. Annu. Rev. Biomed. Eng., 19, 1 (2017). DOI: 10.1146/annurev-bioeng-071516-044442 [28] T. Würfl, M. Hoffmann, V. Christlein, et al., Deep learning computed tomography: Learning projection-domain weights from image domain in limited angle problems. IEEE Trans. Med. Imaging, 37, 6 (2018). DOI: 10.1109/TMI.2018.2833499 [29] L.T. Yang, R.J. Ge, S.C. Feng, et al., Learning projection views for sparse-view ct reconstruction. Proceedings of the 30th ACM international conference on multimedia, pp. 2645–2653 (2022). [30] H, Lee, J. Lee, H. Kim, et al., Deep-neural-network-based sinogram synthesis for sparse-view CT image reconstruction. IEEE Trans. Radiat. Plasma Med. Sci., 3, 2 (2018). DOI: 10.1109/TRPMS.2018.2867611 [31] B. Guan, C. Yang, L. Zhang, et al., Generative modeling in sinogram domain for sparse-view CT reconstruction. IEEE Trans. Radiat. Plasma Med. Sci., 8, 2 (2023). DOI: 10.1109/TRPMS.2023.3309474 [32] K.H. Jin, M.T. McCann, E. Froustey, et al., Deep convolutional neural network for inverse problems in imaging. IEEE Trans. Image Process., 26, 9 (2017). DOI: 10.1109/TIP.2017.2713099 [33] Y. Han, J.C. Ye, Framing U-Net via deep convolutional framelets: Application to sparse-view CT. IEEE Trans. Med. Imaging, 37, 6 (2018). DOI: 10.1109/TMI.2018.2823768 [34] Z.C. Zhang, X.K. Liang, x. Dong, et al., A sparse-view CT reconstruction method based on combination of DenseNet and deconvolution. IEEE Trans. Med. Imaging, 37, 6 (2018). DOI: 10.1109/TMI.2018.2823338 [35] J. Gu, J.C. Ye, Multi-scale wavelet domain residual learning for limited-angle CT reconstruction. arXiv preprint arXiv:1703.01382. DOI: 10.48550/arXiv.1703.01382 [36] Y.P. Chan, X. Liu, T.S. Wang, et al., An attention-based deep convolutional neural network for ultra-sparse-view CT reconstruction. Comput. Biol. Med. 161 (2023). DOI: 10.1016/j.compbiomed.2023.106888 [37] C.L. Ma, Z.L. Li, Y. Zhang, et al., Medical Image Computing and Computer Assisted Intervention -MICCAI 2023. (Springer Nature Switzerland), pp. 250–259 [38] C. Yang, D. Sheng, B. Yang , et al., A dual-domain diffusion model for sparse-view CT reconstruction. IEEE Signal Process. Lett. (2024). DOI: 10.1109/LSP.2024.3392690 [39] J. Liu, Anirudh R, Thiagarajan J J, et al., Proceedings of the IEEE/CVF International conference on computer vision, (Paris, France, 2–6 Oct. 2023) [40] H.Chen, Y. Zhang, Y. Chen, et al., LEARN: Learned experts' assessment-based reconstruction network for sparse-data CT. IEEE Trans. Med. Imaging. 37.6 (2018). DOI: 10.1109/TMI.2018.2805692 [41] B. Zhou, X. Chen, S.K. Zhou, et al., DuDoDR-Net: Dual-domain data consistent recurrent network for simultaneous sparse view and metal artifact reduction in computed tomography. IEEE Trans. Med. Image Anal. 75 (2022). DOI: 10.1016/j.media.2021.102289 [42] J. Liu, Anirudh R, Thiagarajan J J, et al., Improving generalizability in limited-angle ct reconstruction with sinogram extrapolation. Medical Image Computing and Computer Assisted Intervention–MICCAI 2021: 24th International Conference, (Strasbourg, France, September 27–October 1, 2021) [43] D.L. Hu, J. Liu, T.L. Lv, et al., Hybrid-domain neural network processing for sparse-view CT reconstruction. IEEE Trans. Radiat. Plasma Med. Sci. 5, 1 (2020). DOI: https://doi.org/10.1109/TRPMS.2020.3011413 [44] C.

Wang, K. Shang, H. Zhang, et al., DuDoTrans: dual-domain transformer provides more attention for sinogram restoration in sparse-view CT reconstruction. arXiv preprint arXiv:2111.10790 (2021). DOI: 10.48550/arXiv.2111.10790 [45] Parker,D.L., Optimal short scan convolution reconstruction for fan beam CT. Med. Phys. 9.2 (1982). DOI: 10.1118/1.595078 [46] P. Liu, H. Zhang, K. Zhang, et al., Multi-level wavelet-CNN for image restoration. CVPRW. (2018). DOI: 10.48550/arXiv.1805.07071 [47] K. Baete, J. Nuyts, K. Van Laere, et al., Evaluation of anatomy based reconstruction for partial volume correction in brain FDG-PET. Neuroimage. 23.1 (2004). DOI:10.1016/j.neuroimage.2004.04.041 [48] K. Vunckx, A. Atre, K. Baete, et al., Evaluation of three MRI-based anatomical priors for quantitative PET brain imaging. IEEE Trans. Med. Imaging. 31.3 (2011). DOI:10.1109/TMI.2011.2173766 [49] N. Burgos, MJ. Cardoso, K. Thielemans, et al., Attenuation correction synthesis for hybrid PET-MR scanners: Application to brain studies. IEEE Trans. Med. Imaging. 33.12 (2014). DOI:10.1109/TMI.2014.2340135 [50] E. Meyer, R. Raupach, M. Lell, et al., Normalized metal artifact reduction (NMAR) in computed tomography. Med. Phys. 37.10 (2010). DOI:10.1118/1.3484090 [51] AH Andersen, AC Kak, Simultaneous algebraic reconstruction technique (SART): a superior implementation of the ART algorithm. Ultrason. Imaging. 6.1 (1984). DOI:10.1177/016173468400600107 [52] M. Jiang, G. Wang., Convergence of the simultaneous algebraic reconstruction technique (SART). IEEE Trans. Image Process. 12.8 (2003). DOI:10.1109/TIP.2003.815295 [53] R. Gordon., A tutorial on ART (algebraic reconstruction techniques). IEEE Trans. Nucl. Sci. 21.3 (1974). DOI:10.1109/TNS.1974.6499238 [54] EY Sidky, CM Kao, X. Pan., Accurate image reconstruction from few-views and limited-angle data in divergent-beam CT. J. X-Ray Sci. Technol. 14.2 (2006). DOI:10.3233/XST-2006- [55] J. Dai, H. Qi, Y. Xiong, et al., Deformable convolutional networks. Proceedings of the IEEE international conference on computer vision, (pp. 764-773). [56] W. Yu, P. Zhou, S. Yan, et al., Inceptionnext: When inception meets convnext. Proceedings of the IEEE/cvf conference on computer vision and pattern recognition, (pp. 5672-5683). [57] C. Szegedy, S. Ioffe, V. Vanhoucke, et al., Inception-v4, inception-resnet and the impact of residual connections on learning. Proceedings of the AAAI conference on artificial intelligence, (Vol. 31, No. 1). [58] C. Kim, Y. Kyriakou, T. Riedel, et al., Data consistency-driven scatter kernel optimization for x-ray cone-beam CT. Phys. Med. Biol. 60.15 (2015): 5971–5992. DOI:10.1088/0031-9155/60/15/5971 [59] Y. Kyriakou, T. Riedel, W.A. Kalender, et al., Combining deterministic and Monte Carlo calculations for fast estimation of scatter intensities in CT. Phys. Med. Biol. 51.18 (2006): 4567–4586. DOI:10.1088/0031-9155/51/18/008 [60] P. Qin, G. Lin, X. Li, et al., A correlated sampling-based Monte Carlo simulation for fast CBCT iterative scatter correction. Med. Phys. 50.3 (2023): 1466–1480. DOI:10.1002/mp.16073 [61] B. Iskender, Y. Bresler, A physics-motivated DNN for X-ray CT scatter correction. Proc. IEEE 17th Int. Symp. Biomed. Imaging (ISBI) (2020): DOI:10.1109/ISBI45749.2020.9098512 [62] B. Iskender, Y. Bresler, Scatter correction in X-ray CT by physics-inspired deep learning. IEEE Trans. Comput. Imaging 8 (2022): 1074–1088. DOI:10.1109/TCI.2022.3226300 [63] J. Pautasso,

M. Caballo, M. Mikerov, et al., Deep learning for X-ray scatter correction in dedicated breast CT. Med. Phys. 50.4 (2023): 2022-2036. DOI:10.1002/mp.16185